Journal of Materials Chemistry A

A Prototype of High-Performance Two-Electron Non-aqueous Organic Redox Flow Battery Operated at -40 °C

Journal:	*Journal of Materials Chemistry A*
Manuscript ID	TA-ART-10-2022-007876.R1
Article Type:	Paper
Date Submitted by the Author:	24-Oct-2022
Complete List of Authors:	Liang, Zhiming; University of Kentucky, Jha, Rahul; University of Kentucky, Suduwella, Thilini; McGill University, Chemistry Attanayake, N.; University of Kentucky, Chemistry Wang, Yangyang; University of Colorado Boulder Zhang, Wei; Alfred University, School of Engineering Cao, Chuntian; Brookhaven National Laboratory Kaur, Aman Preet; University of Kentucky, Department of Chemistry; University of Kentucky, Department of Materials and Chemical Engineering Landon, James; University of Kentucky Center for Applied Energy Research Odom, Susan; University of Kentucky, Chemistry

A Prototype of High-Performance Two-Electron Non-aqueous Organic Redox Flow Battery Operated at -40 °C

Zhiming Liang[1,3]*, Rahul Kant Jha[1], Thilini M. Suduwella[1,2], N. Harsha Attanayake[1,2], Yangyang Wang[3], Wei Zhang[3], Chuntian Cao[4], Aman Preet Kaur[1,2], James Landon[5,6], and Susan A. Odom[1,2]

[1] Department of Chemistry, University of Kentucky, Lexington, KY 40506, USA
[2] Joint Center for Energy Storage Research, Lexington, KY 40506, USA
[3] Department of mechanical Engineering, University of Colorado, Boulder, CO 80309, USA
[4] Computational Science Initiative, Brookhaven National Laboratory, Upton, NY 11973, USA
[5] Center for Applied Energy Research, University of Kentucky, Lexington, KY 40511, USA
[6] Department of Chemical and Materials Engineering, University of Kentucky, Lexington, KY 40506, USA

* Corresponding author information
leungchiminh@gmail.com

Abstract

Redox flow batteries (RFBs) which can be operated under subzero temperature is significant for applications in cold regions. However, very few of RFBs have been reported to use below -20 ℃. Problems with active materials, such as low solubility, poor stability, and high viscosity are the major difficulties to overcome. Here, we report a prototype of ultra-low temperature (-40 ℃) non-aqueous RFB, using two-electron glycolated phenothiazine and viologen as posolyte and negolyte which successfully completed 100 cycles at 15 mA cm^{-2}. The cell which was assembled with 0.1 mol L^{-1} active materials exhibited a theoretical voltage of 1.9 V, an average discharge volumetric capacity of 3.2 A h L^{-1}, and *ca.* 78% capacity retention over 100 cycles. When the active materials concentration was increased to 0.25 mol L^{-1}, the discharge volumetric capacity reached *ca.* 8.5 A h L^{-1}. This marks the first time that non-aqueous redox flow cells have been long-term cycled at high current density at ultra-low temperature.

1. Introduction

Grid energy storage plays a pivotal role in the smooth and metered delivery of electricity from variable resources with uncontrollable intermittency and are mismatched in electricity supply versus grid user demand.[1, 2] Secondary batteries that store energy in solid electrodes (e.g., lithium-ion batteries) or in active species dissolved in electrolytes (e.g., redox flow batteries) can be used to supply controllable and consistent electricity to the electrical grid.[3-5] The essential performance of these batteries for the application under consideration means sensitivity to temperature must be addressed.[6-10] Redox flow batteries (RFBs) which can be operated under subzero temperature are significant for applications in cold regions. However, to date, very few of RFBs are reported to use below -20 ℃. Low temperature operation of rechargeable batteries is a challenge due to the low solubility, poor stability, low ionic conductivity, and sluggish kinetics of electrolytes.[11, 12] Ion-exchange membranes (IEMs) typically used in RFBs usually lead to high cell resistances when the temperature drops to subzero. With these limitations, operation below 0 ℃ is difficult to support. Therefore, the development of low-temperature-tolerant batteries is essential for use in variable environmental conditions.

So far, most of the low temperature battery research has been conducted on lithium-ion batteries.[10-15] NASA and other agencies have worked on a suite of exotic liquid phase batteries, but none have proven commercially viable.[16-20] In addition to decreased ionic conductivity, a major concern of low temperature solid-state batteries is the integrity of electrode materials.[21, 22] Compared to lithium-ion batteries, limited research has been done on ultra-low temperature RFBs. One difficulty for assembling and cycling RFBs is that most flow cells contain aqueous electrolytes, and the solvent freezes as the temperature drops to sub-zero temperature.[23-25] Another problem is the compatibility and durability of the components used in RFBs such as the flexible tubing used to pump electrolytes and the O rings used to seal the cells. As the

temperature drops, these polymers lose flexibility, leading to electrolyte leakage or pumping failure. Few groups reported aqueous inorganic flow battery which cycled at *ca.* -20 °C (Table S1).[26-28] However, a drawback of this aqueous battery system is the limited cell voltage due to the solvent (H_2O electrochemical window is ~ 1.23 V). Ma *et al.* reported a porphyrin-based non-aqueous symmetric cell which could cycle at -40 °C.[29] Yet, the cycling rate was as low as 1 mA cm^{-2} which needed ~ 100 hours to finish one cycle charge/discharge.

Despite the potential problems of low temperature RFBs, they are worth further pursuit due to recent, significant developments in highly stable and soluble redox active molecules.[30-32] At any temperature, they pose advantages in stationary storage due to their decoupled power and energy scaling, simplified manufacturing, long service lifetime, and relatively easy maintenance.[31, 33-35] Several types of redox active materials have been investigated for non-aqueous redox flow batteries (NAqRFBs) such as organic molecules,[36-44] redox active macromolecules,[45-47] and metal coordination complexes.[48-50] For many active materials used in NAqRFBs, either their solubilities (< 1 mol L^{-1}) or redox potentials (< 1.5 V) result in limitations in energy density. The limitations are exacerbated for low temperature RFBs as the solubilities decrease when temperature drops. Thus, it is important to develop new redox active materials with high solubilities and potential for applications at ultra-low temperature. Molecular engineering has been widely applied to optimize molecules solubility, redox potential, electrochemical stability, and ionic conductivity *etc*.. However, only a few of molecular cores show promising potential as redox active materials, including pososlytes (e.g., phenothiazine,[36, 51, 52] phenazine,[38, 53] and quinone[54, 55] derivatives) and negolytes (e.g., viologen derivatives[56, 57]).

In this manuscript, glycolated phenothiazine (BMEEOEPT) and Viologen (MEEV-$TFSI_2$) were synthesized as posolyte and negolyte, respectively, to assemble full cells (Figure 1). This two-electron transfer NAqRFB can operate at temperatures as low as *ca.* -40 °C with a moderately high current density (15 mA cm^{-2}) for long-term cycling (> 100 cycles). The solubility of pristine BMEEOEPT is miscible with organic electrolytes, and MEEV-$TFSI_2$ is soluble at room temperature to at least 1.0 M. They are soluble to at least 0.25 M at -40 °C (Table 1). These values are among the best solubilities reported for stable, scalable NAqRFB materials.[58-61] Furthermore, the two-electron transfer reaction enables a larger theoretical cell voltage (*ca.* 1.9 V), almost twice that of the one-electron reaction. Using tailored flow cell components (Figure 1 and Figure S2), we evaluated BMEEOPT and MEEV-$TFSI_2$ in a flow cell prototype at 25 °C and at -40 °C. Here we report screening by cyclic voltammetry, flow cell cycling results, and post-cycling electrolyte analysis.

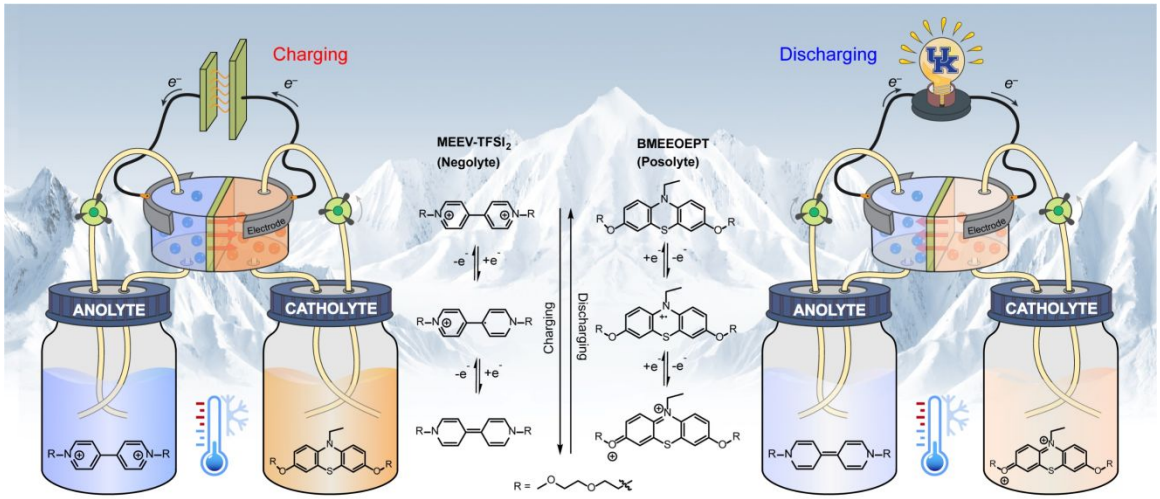

Figure 1. Illustrative design of an ultra-low temperature redox flow battery during charging and discharging. During charging, MEEV-$TFSI_2$ is reduced and BMEEOEPT is oxidized. The solubilizing glycol R group shown at the bottom of the image is common to both molecules.

2. Experimental section

2.1 Materials and synthesis

Acetonitrile (ACN, 99.9%, anhydrous) was purchased from J.T.Baker and used from a solvent delivery system (LC Technology Inc). Tetraethylammonium bis(trifluoromethylsulfonyl)imide (TEATFSI, >98%) was purchased from Iolitec. Daramic 175 microporous polymer separator (175 µm, porosity is 58%, and mean pore size is 100 nm) was purchased from Daramic LLC. FAPQ 375 PP anion exchange membrane (75 µm) was purchased from Functional Membranes and Plant Technology (FumaTech). All membranes and separators were soaked in 0.5 M TEATFSI/ACN for at least 24 h before employing them in flow cell experiments. Room temperature flow cells were conducted in an Argon atmosphere glovebox (MBraun, O_2 < 5 ppm, H_2O < 0.1 ppm). -40 °C flow cells were assembled in Argon-filled glovebox and cycled in a freezer which located in the air. N-ethyl-3,7-bis(2-(2-methoxyethoxy)ethoxy)phenothiazine (BMEEOEPT) and bis(2-(2-methoxyethoxy)ethyl)viologen bis(bis(trifluoromethanesulfonyl)imide) (MEEV-$TFSI_2$) were prepared using reported procedures.[58,62]

2.2 Solubility test

The solubilities of BMEEOEPT and MEEV-$TFSI_2$ in ACN and 0.5 M TEATFSI/ACN were determined by a shake-flask method. Aliquots of test solvent (50 -100 µL) were slowly added to each active material (80 – 110 mg) and stirred between additions to obtain saturated solution as determined by visual inspection. The components were measured to record their weight and volume, leading to a calculation of the density of solution. The calculated density was then used to determine the real volume of samples. For the low temperature solubility, we prepared a series of calculated concentration solutions and kept the solutions at -40 °C for 48 hours. Precipitation was determined by visual inspection at -40 °C.

2.3 Cyclic voltammetry

Cyclic voltammetry (CV) experiments were conducted using a CH instruments 650E potentiostat. Glassy carbon (3 mm diameter) was employed as the working electrode, platinum wire as the counter electrode, and an un-fritted freshly anodized Ag/AgCl wire as the reference electrode. Decamethylferrocene was used as an internal reference, and redox potentials are reported with respect to ferrocene/ferrocenium ($Cp_2Fe^{0/+}$). 100% solution resistance compensation or iR correction was applied. Ferrocene was added as internal reference (~10 µM). Half-wave redox potentials ($E^{1/2}$) were calculated by the average of peak reduction and oxidation potentials. Peak current ratios (ip,ox/ip,red) were calculated by dividing the oxidation current by the reduction current. A scan rate of 100 mV s^{-1} (started from 0V to +V then to -V) was used in voltammograms that were analyzed to determine redox potential, peak separation, and peak current ratios. For -40 °C measurement, the electrolytes were kept in -40 °C for 12 hours before CV was conducted.

2.4 Randel-Sevcik Analysis to Obtain Diffusion Coefficients

Diffusion coefficients were calculated by using the Randles-Sevcik analysis[63] at scan rates of 25, 50, 75, 100, 200, 300, 400, and 500 mV s^{-1} using equation 1.

$$i_p = 0.4463\, nFAc\left(\frac{nFD}{RT}v\right)^{0.5} \qquad \text{(Equation 1)}$$

Where i_p is the peak current (A), n is the number of electrons transferred (-), F is the Faraday constant (96,485 C mol^{-1}), A is the electrode area (cm^2), c is the concentration (mol cm^{-3}), D is the diffusion coefficient (cm^2 s^{-1}), R is the gas constant (8.314 J mol^{-1} K^{-1}), T is the absolute temperature (K), and v is the scan rate (V s^{-1}).

2.5 Flow cell cycling

Small volume custom flow cells with interdigitated flow fields were used during redox flow cell cycling.[64] The backing plates were made from polypropylene. 3.18 mm thick impregnated graphite was used to make the graphite flow fields (product G347B, MWI Inc., Rochester, NY). Carbon paper (SGL 29 AA, 190 ± 30 µm thickness, SGL group, Wiesbaden, Germany) was cut to 1.7 cm × 1.5 cm and used as received. One piece of carbon paper was layered on either side of the membrane (FAPQ 375 PP, Fuma-Tech) or separator (Daramic 175, Daramic LLC). The cells were sealed using custom gaskets cut from polytetrafluoroethylene gasket tape (Goretex) with an area of 2.55 cm^2. All flow cell bodies were assembled in the air and then dried in the vacuum oven (room temperature, pressure -100 kPa) for 1 h before being transferred into an argon-filled glovebox (MBraun, O_2 < 5 ppm, H_2O < 0.1 ppm).

Perfluoroalkoxyalkane (PFA) jars (10 mL, Savillex) were used as electrolyte reservoirs, and a peristaltic pump (Masterflex L/S Series) was used to carry the electrolyte at a flow rate of 10 mL min^{-1}. Norprene tubing (Masterflex) was used inside the pump head. PFA tubing (Swagelok) connected the reservoirs to the flow cell. Stainless steel compression fittings (Swagelok) were used to connect the Norprene and PFA tubing. The inner diameter of all tubing was 1.6 mm. Ultra-low temperatures and organic solvents resistance O-rings were purchased from McMaster. The electrolyte used for flow cycling in this study was 0.5 M TEATFSI in ACN. The 25 and -40 °C flow cells contained 0.1 M BMEEOEPT and 0.1 M MEEV-$TFSI_2$ in 0.5 M TEATFSI/ACN on both sides, and the solutions were separated by a Daramic 175 separator. The ultra-low temperature flow cells were kept at -40 °C for 24 hours before Galvanostatic cycling.

3. Results and discussion

3.1 Molecular engineering

Molecules containing phenothiazine core are excellent cathode materials used in organic redox flow battery. To exploit the maximum concentration of these redox active phenothiazine derivatives, we investigated a series of phenothiazine derivatives to study the effect of side chains on solubility. Figure S1 shows the solubility study of phenothiazines (and radicals) with different side chains. Oligoglycol chains can effectively improve the solubility of phenothiazine in both neutral and radical states. When incorporate oligoglycol chains with viologen core which is a promising anode material for redox flow battery, both the solubility and electrochemical stability are enhanced.[51] The solubility of pristine BMEEOEPT is miscible with organic electrolytes, and MEEV-$TFSI_2$ is soluble at room temperature to at least 1.0 M. They are soluble to at least 0.25 M at -40 °C (Table 1). These values are among the best solubilities reported for stable, scalable NAqRFB materials.[58-61] Furthermore, the two-electron transfer reaction enables BEEOEPT/MEEV-$TFSI_2$ redox couple a larger theoretical cell voltage (*ca.* 1.9 V) which is also among the high work potentials in RFBs.

Table 1. Solubility of redox active species at 25 and -40 °C. Except for the compound labeled as miscible, solubility values reported here are minimum values. (0.1M premixed stands for 0.1M BMEEOEPT + 0.1M MEEV-$TFSI_2$)

Electrolyte concentration in 0.5 M TEATFSI/ACN	Solubility at 25 °C	Solubility at -40 °C
0.1 M premixed	soluble	soluble
0.2 M premixed	soluble	soluble
0.3 M premixed	soluble	insoluble
0.4 M premixed	soluble	insoluble
BMEEOEPT	miscible	0.25 M
MEEV-$TFSI_2$	1.0 M	0.25 M

3.2 Electrochemical characterization

To calibrate their performance for flow cell cycling studies, cyclic voltammograms (CV) were recorded for both active materials at 1 mM in 0.5 M TEATFSI in acetonitrile (ACN) at both 25 and -40 °C (Figure 2). ACN and TEATFSI was used by considering the melting point, viscosity, and electrolyte conductivity (Table S2).[51, 52] The voltammograms are calibrated to ferrocene/ferrocenium ($Cp_2Fe^{0/+}$) at 0 V. Decamethylferrocene was used as an internal reference due to the first redox peak of ferrocene/ferrocenium overlaps with BMEEOEPT *versus* Ag/AgCl electrode (Figure S3). At 25 °C, the position of the second redox potentials, reported in Table 2, occur at 0.69 V for BMEEOEPT and -1.21 V for MEEV-$TFSI_2$ versus $Cp_2Fe^{0/+}$. The positions of the peaks shifted by less than 0.2 V when the temperature is reduced to -40 °C. When both the second oxidation of BMEEOEPT and second reduction of MEEV-$TFSI_2$ are accessed, the theoretical cell voltage is 1.90 V at 25 °C, dropping slightly to 1.84 V at -40 °C. The redox events are reversible, with peak-to-peak separations of the second redox event at 57 mV at 25 °C and slightly lower at -40 °C. The diffusion coefficients estimated by Randles-Sevcik analysis (Figure S4c) of variable scan rate voltammograms are *ca.* two times larger at 25 °C than at -40 °C,[63] which is presumably due to increased solution viscosity at lower temperatures.

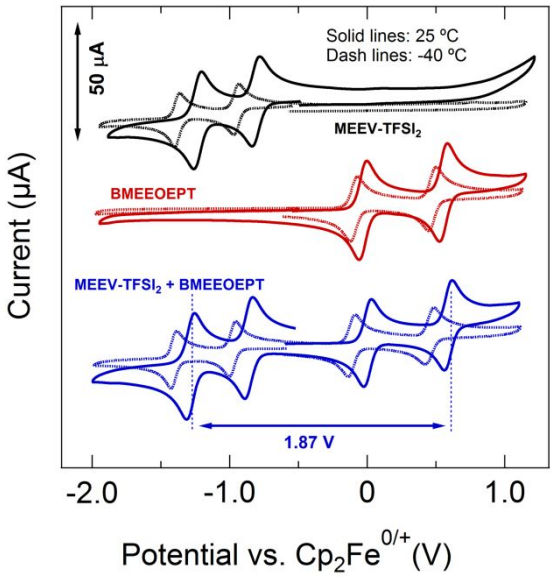

Figure 2. Cyclic voltammograms of electrolytes at 25 °C (solid lines) and at -40 °C (dashed lines) of MEEV-$TFSI_2$ (black), BMEEOEPT (red), and a 1:1 combination of the two (blue) at 1 mM in 0.5 M TEATFSI/ACN, referenced to ferrocene/ferrocenium at 0 V. The scan rate is 100 mV s^{-1}.

Table 2. Electrochemical data of BMEEOEPT and MEEV-$TFSI_2$ in 0.5 M TEATFSI/ACN at 25 °C and -40 °C. The half wave redox potentials were calibrated to ferrocene/ferrocenium ($Cp_2Fe^{0/+}$) using decamethylferrocene as the internal reference.

Compound	Half-wave redox potential vs $Cp_2Fe^{0/+}$ (V)				Peak current ratio ($i_{p,ox}/i_{p,red}$)				Peak separation (mV)				Diffusion Coefficient (x10^{-6} cm^2 s^{-1})			
	25 °C		-40 °C		25 °C		-40 °C		25 °C		-40 °C		25 °C		-40 °C	
	1st	2nd	1st	2nd	1st	2nd	1st	2nd	1st	2nd	1st	2nd	1st	2nd	1st	2nd
MEEV-$TFSI_2$	-0.79	-1.21	-0.81	-1.24	1.22	1.03	1.18	1.05	59	57	54	54	6.99	9.15	1.56	4.41
BMEEOEPT	0.10	0.69	0.04	0.60	1.22	1.03	1.18	1.08	59	57	50	43	10.8	10.9	4.59	4.02

3.3 Flow cell cycling

Membrane and separator characteristics play a critical role in redox flow cells electrochemical performance. Their properties govern the transport of supporting electrolyte between negative and positive sides of the cell to maintain electroneutrality, as well as determining the selectivity and rate of redox active species crossover. Large ohmic resistances and low ionic conductivities of membranes and separators decrease the upper limits for charging rates. According to our previous studies, cells assembled with ion-selective membranes can operate at twice the average capacity achieved with non-selective separators at room temperature.[52] However, as temperature drops to as low as -40 °C, the ohmic resistance of ion-selective membranes in electrolyte can increase by several orders of magnitude. Figure S5a shows the electrochemical impedance spectroscopy (EIS) of two FAPQ 375 pp anion exchange membranes at 25°C and -40°C where the ohmic resistance increased from *ca.* 12 Ω (25 °C) to 1100 Ω (-40 °C). This large resistance prevents RFBs from operating at high current density (e.g., >5 mA cm^{-2}). For this reason, we set up our ultra-low temperature flow cells using non-selective separator Daramic 175 with larger pore size (100 nm) but smaller ohmic resistance shift (*ca.* 2.5 Ω as temperature drops to -40 °C) (Figure S5b). In this cell, the crossover rate of active species is sufficiently fast that separating them is not worthwhile. Therefore, we premixed the electrolytes so that each electrolyte contained equal amounts of MEEV-$TFSI_2$ and BMEEOEPT.

The flow cells were assembled with each reservoir containing 10 mL of 0.1M premixed BMEEOEPT and MEEV-$TFSI_2$ in 0.5M TEATFSI/ACN yielding a theoretical capacity of 5.36 A h L^{-1} at both temperatures. A potential window of 0.6 V to 2.2 V and different current densities (10, 15, 20, and 30 mA cm^{-2}) (Figure S6) was conducted to determine trends in current density, accessible capacity, electrochemical efficiency, and overpotential. Figure 3a and Table S3 show a comparison of coulombic, voltage, and energy efficiency at different current densities. Within the same temperature, the coulombic efficiency increases, and voltage efficiency decreases with increasing current density due to slower crossover rate and larger cell polarization. Compared within the same current, the cell run at -40 °C has *ca.* 15% higher coulombic efficiency than the 25 °C cell. The increased coulombic efficiency suggests that the side reactions (crossover, self-discharge *etc*.) is effectively hindered at ultra-low temperature. The difference between the two temperature decreases at a higher current rate (e.g., *ca.* 5% at 30 mA cm^{-2}). Considering a balance between charging rates and accessing percent of the capacity, 15 mA cm^{-2} was applied for long-term galvanostatic cycling (Figure 3c and 3d). At 25 °C, the cell initial discharge capacity is 4.28 A h L^{-1} and decreases to 2.63 A h L^{-1} after 100 cycles. The capacity fade is likely because: i) unbalanced electrolyte concentrations, and ii) molecules degradation. An unbalanced cell which either caused by a mismatch in

electrolyte volume or active materials concentrations can exacerbate the cell polarization and reduce the accessed capacities.[58] Acetonitrile, which was applied as the solvent for the cells, has a relatively low boiling point (Table S2). This low boiling point enables acetonitrile easily to evaporate through the connections among reservoirs and tubes after long-term cycling which will more likely cause unbalanced electrolyte volume in reservoirs. Furthermore, the use of non-selective Daramic 175 separator could increase the concentration mismatch of the respective active species, especially for two-electron transfer molecules (a third plateau formed as shown in Figure 3b).[58] To figure out, the posolyte and negolyte were rebalanced after 100 cycles (the 25°C cell). The discharge capacity of the 101th cycle recovered from 2.63 to 3.17 A h L^{-1} (a 21% increase) which suggests that unbalanced concentration is partly responsible for capacity fade. For the cell cycled at -40°C, the discharge capacities are 3.43 and 2.66 A h L^{-1} for the 1st and one 100th cycles, respectively. The first discharge capacity is *ca.* 20% lower than the 25 °C cell which is attributed to the decreased ion transport and increased cell polarization (Figure 3b). The capacity retention reaches 77.6% after 100 cycles, which is higher than 61.4% (the 25 °C cell). As discussed, unbalanced electrolyte concentrations play a key role in cell capacity loss. The slow capacity decay for -40 °C could be explained by the fact that the active species mismatch will be effectively inhibited as temperature goes to ultra-low. The -40°C cell was moved out of the freezer and cycled a few more cycles at room temperature. The average discharge capacity increased to *ca.* 3.8 A h L^{-1} which is slightly lower than the 1st cycle discharge capacity of the 25 °C cell. As further increase the concentration of active materials to 0.25 M, the average accessible discharge capacity of 30 cycles reached 8.6 ± 0.7 A h L^{-1} at -40 °C which marks the highest volumetric capacity under subzero temperature (Figure S7 and Table S1).

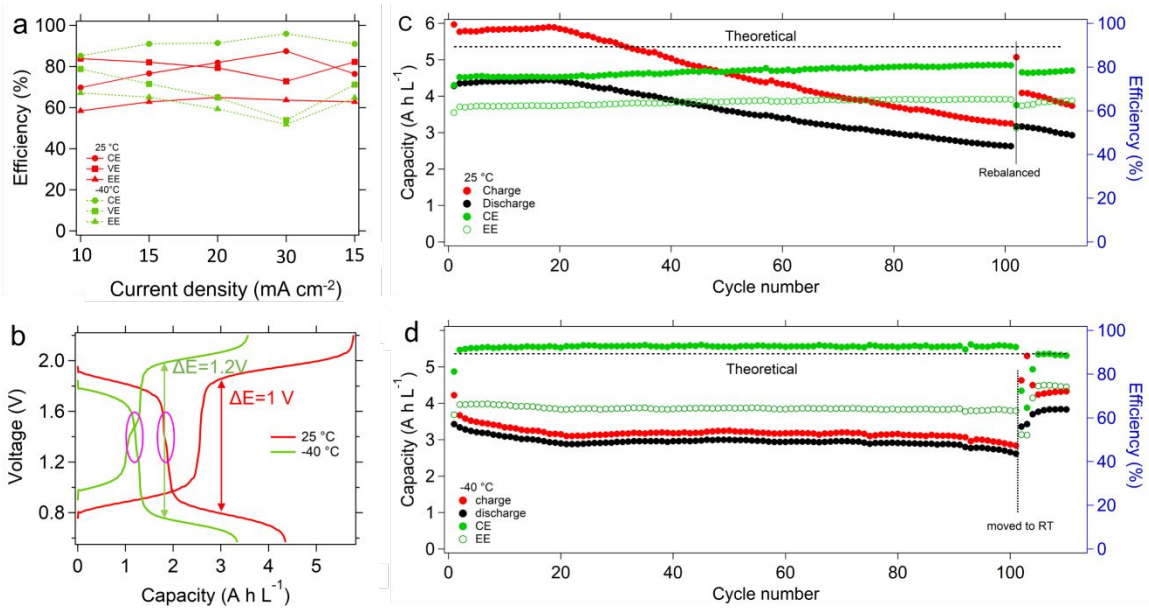

Figure 3. Electrochemical performance of 0.1 M premixed RFBs cycled at 25 and –40 °C with Daramic 175 separator. Each cell contains 0.1 M BMEEOEPT and 0.1 M MEEV-TFSI$_2$ in both posolyte and negolyte. All redox active species dissolved in 0.5 M TEATFSI/ACN. a) Comparison of Coulombic, voltage and energy efficiencies at current densities of 10, 15, 20, 30, and 15 mA cm^{-2}; b) The 2nd cycle voltage versus capacity profile for long-term cycling at a current rate of 15 mA cm^{-2}; c) Long-term cycling of the 25 °C cell; d) Long-term cycling of the -40 °C cell. The current rate for c) and d) is 15 mA cm^{-2}.

3.4 Post-cycling analysis

Electrochemical impedance spectroscopy (EIS) was used to characterize the cell resistance. The ohmic resistance (R_1) of the 25 °C cell does not change after 100 cycles (Figure 4a and Table S4). The charge transfer resistance (R_2) decreases from 2.74 to 0.14 Ω. For the -40 °C cell, the ohmic resistance increases to 2.79 Ω which is slightly higher than the pre-cycle value 2.11 Ω (Figure 4b and Table S4). After the cell was moved to 25 °C and cycled for 10 cycles, the cell ohmic resistance drops to 1.63 Ω. These changes suggest that there may be some unexpected precipitation of active materials on the surface of carbon paper electrode at ultra-low temperature. The precipitates dissolve when moved to room temperature. The voltage efficiency of the two cells shown in Figure 4c is consistent with the change in ohmic resistance of the cells.

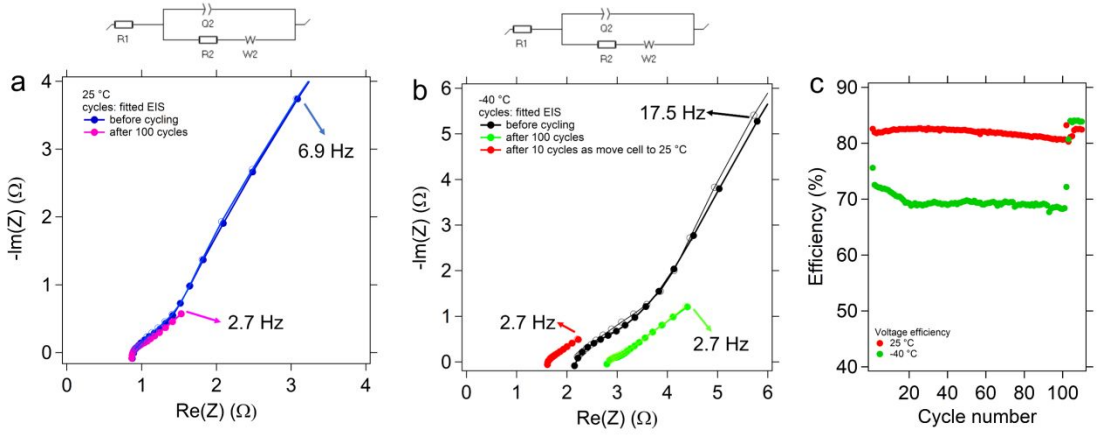

Figure 4**.** Electrochemical impedance spectroscopy (EIS) measurement (dots) and fitting curves (circles) of 0.1M premixed BMEEOEPT and MEEV-$TFSI_2$ RFBs with Daramic 175 separators. a) EIS of the 25 °C cell before and after 100 cycles; b) EIS of the -40 °C cell before, after 100 cycles, and after 10 cycles as moved the cell to 25 °C; c) Comparison of voltage efficiency for long-term cycling of both cells. EIS was conducted with circulating electrolytes at open circuit potential with an amplitude of 10 mV in a frequency range of 100 kHz to 1 Hz (5 steps per decade). The area of carbon paper electrode: 2.55 cm^2. The plot above a and b is the equivalent circuit model.

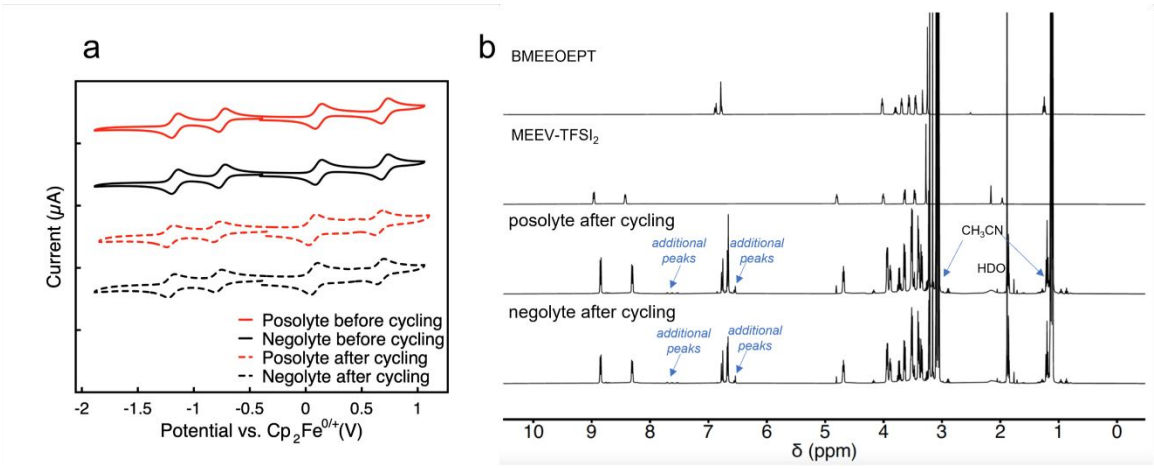

Figure 5**.** CV and ^1H NMR analysis of 0.1M premixed RFBs cycled at -40 °C with Daramic 175 separator. a) CV of pristine and cycled posolyte and negolyte; b) ^1H NMR spectra of posolyte and negolyte before and after cycling (CD_3CN, 400 MHz).

To further determine the electrochemical stability of the two redox active materials, we analyzed the electrolyte solutions by CV (Figure 5a and SI Figure S8) and ^{1}H NMR (Figure 5b, SI Figure S9, and S10). CV shows that no new redox active species are generated during cycling. Both electrolytes are the same before and after cycling. To prepare the NMR solutions, excess sodium thiosulfate was added to quench residual oxidized BMEEOEPT, and the solution was filtered to remove this solid after which the materials were concentrated to remove solvent before dissolution in ACN-d_3. Air was bubbled through the solutions to quench residual reduced viologen. A few less intense, new peaks (Figure 5b) were observed in the aromatic region of ^{1}H NMR for the cycled posolyte and negolyte. We believe that these additional peaks were generated due to the partial decomposition of BMEEOEPT which led to the observed capacity degradation in the ultra-low cell cycling. As the -40 °C cells were cycled in air due to the special temperature requirements after assembled inside an argon-filled glovebox, atmospheric oxygen may leak into electrolytes (e.g. connections among tubes, reservoirs, and flow cell body; or mechanical abrasion of the tubes)[65] which could cause the partial degradation of BMEEOEPT. Our previous study has found that these two redox active molecules are stable for hundreds of cycles in inert environment.[58] However, the phenothiazine derivatives could be oxidized to form sulfoxides and sulfones under aerobic conditions.[66, 67] As shown in the proposed mechanism for BMEEOEPT degradation (scheme 1a), charged BMEEOEPT turns into its sulfoxide sulfone form by reacting with oxygen. Besides, viologen$^{\cdot+}$ can be oxidized to viologen^{2+} with oxygen which also lead to capacity loss.[65] The ^{1}H NMR spectra of another flow cell which cycled at 25 °C does not show additional peaks after 70 cycles (Figure S11). Thus, it confirms that reactions of redox active materials with oxygen contribute to the observed capacity fade of the low temperature flow cell cycling.

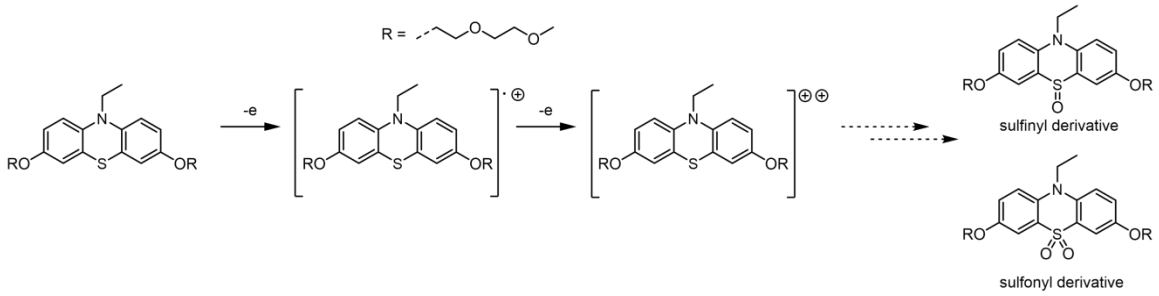

Scheme 1. Plausible pathways for BMEEOEPT decomposition in aerobic conditions.

Conclusion

In summary, 0.1 M premixed BMEEOEPT (posolyte) and MEEV-TFSI$_2$ (negolyte) RFBs in 0.5M TEATFSI/ACN with Daramic 175 separator were tested at 25 and -40 °C. The -40 °C cell demonstrated a discharge capacity (1st cycle) of 3.43 A h L^{-1} and a capacity retention of 77.6% after 100 cycles, which are *ca.* 20% lower and 25% higher than the 25 °C cell, respectively. As the active materials concentration is increased to 0.25M, the 30 cycles average accessible discharge capacity of the -40 °C cell reaches 8.6 ± 0.7 A h L^{-1}. The capacity fade is likely due to the mismatch of active species and the degradation of molecules in ambient atmosphere. At -40 °C, the active species mismatch alleviates, which enables stable long-term cycling. The two active molecules are electrochemically stable under an inert environment; however, degradation could happen in ambient atmosphere. ^{1}H NMR analysis shows that the cycled electrolytes at -40 °C have a few less intense, additional peaks in the aromatic region due to unavoidable exposure to the oxygen. Thus, it is necessary to exploit redox active cores which are stable in the air. Molecules designed for aqueous RFBs are good candidates, but the operating voltage of aqueous RFBs is limited due

to the narrow electrochemical stability window of water, so molecular engineering is required to increase the molecules redox potential. Besides, the freezing point of acetonitrile at -45 °C prevents us from further decreasing the cell temperature. Therefore, replacing acetonitrile with other solvents or ionic liquids is of interest in assembling nonaqueous flow cells that operate at even lower temperatures for applications in NASA or in prolonged cold regions of the Earth.

Acknowledgements
We thank the National Science Foundation for funding through the PFI:AIR–TT program (award 1701085), part of the Division of Industrial Innovation and Partnerships. We thank Simon Jones for initial project guidance in the development of low temperature electrolytes for which we received funding from Kentucky NASA. We thank the research group of Fikile Brushett for flow cell components and assistance in cycling protocols.

Footnotes
This work is dedicated in honor and memory of Professor Susan Odom.

References
1. H. Ibrahim, A. Ilinca and J. Perron, *Renewable and Sustainable Energy Reviews*, 2008, **12**, 1221-1250.
2. T. M. Gür, *Energy Environ. Sci*, 2018, **11**, 2696-2767.
3. M. A. Pellow, C. J. M. Emmott, C. J. Barnhart and S. M. Benson, *Energy Environ. Sci*, 2015, **8**, 1938-1952.
4. J. O. G. Posada, A. J. R. Rennie, S. P. Villar, V. L. Martins, J. Marinaccio, A. Barnes, C. F. Glover, D. A. Worsley and P. J. Hall, *Renew. Sust. Energ. Rev.*, 2017, **68**, 1174-1182.
5. Y. Zhang, D. Ma, Z. Chen, A. Iqbal, J. Hu, M. Chen, X. Liu, T. T. Tsega, H. Fazal, P. Xu, F. Tao, J. Zai and X. Qian, *ACS Sustain. Chem. Eng.*, 2022, **10**, 541-551.
6. S. Santhanagopalan, Q. Guo, P. Ramadass and R. E. White, *J. Power Sources*, 2006, **156**, 620-628.
7. H. Lee, M. Yanilmaz, O. Toprakci, K. Fu and X. Zhang, *Energy Environ. Sci*, 2014, **7**, 3857-3886.
8. T. M. Bandhauer, S. Garimella and T. F. Fuller, *J. Electrochem. Soc.*, 2011, **158**, R1.
9. A. Z. Weber, M. M. Mench, J. P. Meyers, P. N. Ross, J. T. Gostick and Q. Liu, *J. Appl. Electrochem.*, 2011, **41**, 1137.
10. M. Alipour, C. Ziebert, F. V. Conte and R. Kizilel, *Batteries*, 2020, **6**, 35.
11. J. Jaguemont, L. Boulon and Y. Dubé, *Appl. Energy*, 2016, **164**, 99-114.
12. G. Zhu, K. Wen, W. Lv, X. Zhou, Y. Liang, F. Yang, Z. Chen, M. Zou, J. Li, Y. Zhang and W. He, *J. Power Sources*, 2015, **300**, 29-40.
13. Y. Yang, Y. Yin, D. M. Davies, M. Zhang, M. Mayer, Y. Zhang, E. S. Sablina, S. Wang, J. Z. Lee, O. Borodin, C. S. Rustomji and Y. S. Meng, *Energy Environ. Sci*, 2020, **13**, 2209-2219.
14. Y. Yang, D. M. Davies, Y. Yin, O. Borodin, J. Z. Lee, C. Fang, M. Olguin, Y. Zhang, E. S. Sablina, X. Wang, C. S. Rustomji and Y. S. Meng, *Joule*, 2019, **3**, 1986-2000.
15. C. S. Rustomji, Y. Yang, T. K. Kim, J. Mac, Y. J. Kim, E. Caldwell, H. Chung and Y. S. Meng, *Science*, 2017, **356**.
16. S. S. Zhang, K. Xu and T. R. Jow, *J. Power Sources*, 2003, **115**, 137-140.
17. M. Smart, B. Ratnakumar and L. Whitcanack, in *6th International Energy Conversion Engineering Conference (IECEC)*, DOI: 10.2514/6.2008-5763.
18. M. C. Smart, B. V. Ratnakumar, A. Behar, L. D. Whitcanack, J. S. Yu and M. Alamgir, *J. Power Sources*, 2007, **165**, 535-543.
19. M. Smart, B. Ratnakumar and S. Surampudi, *J. Electrochem. Soc.*, 2002, **149**, A361.
20. E. Plichta, M. Hendrickson, R. Thompson, G. Au, W. Behl, M. Smart, B. Ratnakumar and S. Surampudi, *J. Power Sources*, 2001, **94**, 160-162.

21. Z. Lin and J. Liu, *RSC Adv.*, 2019, **9**, 34601-34606.
22. F. Zhu, H. Bao, X. Wu, Y. Tao, C. Qin, Z. Su and Z. Kang, *ACS Appl. Mater. Interfaces*, 2019, **11**, 43206-43213.
23. P. Leung, X. Li, C. Ponce de León, L. Berlouis, C. T. J. Low and F. C. Walsh, *RSC Adv.*, 2012, **2**, 10125-10156.
24. C. Zhang, T. S. Zhao, Q. Xu, L. An and G. Zhao, *Appl. Energy*, 2015, **155**, 349-353.
25. J. Pan, M. Huang, X. Li, S. Wang, W. Li, T. Ma, X. Xie and V. Ramani, *Energy*, 2016, **107**, 784-790.
26. F. Ai, Z. Wang, N.-C. Lai, Q. Zou, Z. Liang and Y.-C. Lu, *Nat. Energy*, 2022, **7**, 417-426.
27. B. Li, Z. Nie, M. Vijayakumar, G. Li, J. Liu, V. Sprenkle and W. Wang, *Nat. Commun.*, 2015, **6**, 1-8.
28. Z. Huang, P. Zhang, X. Gao, D. Henkensmeier, S. Passerini and R. Chen, *ACS Appl. Energy Mater.*, 2019, **2**, 3773-3779.
29. T. Ma, Z. Pan, L. Miao, C. Chen, M. Han, Z. Shang and J. Chen, *Angew. Chem. Int. Ed.*, 2018, **57**, 3158-3162.
30. H. Chen, G. Cong and Y.-C. Lu, *J. Energy Chem.*, 2018, **27**, 1304-1325.
31. W. Wang, Q. Luo, B. Li, X. Wei, L. Li and Z. Yang, *Adv. Funct. Mater.*, 2013, **23**, 970-986.
32. J. Luo, B. Hu, M. Hu, Y. Zhao and T. L. Liu, *ACS Energy Lett.*, 2019, **4**, 2220-2240.
33. P. Leung, A. A. Shah, L. Sanz, C. Flox, J. R. Morante, Q. Xu, M. R. Mohamed, C. Ponce de León and F. C. Walsh, *J. Power Sources*, 2017, **360**, 243-283.
34. D. G. Kwabi, Y. Ji and M. J. Aziz, *Chem. Rev.*, 2020,14, 6467–6489.
35. J. Zai, Y. Zhu, K. He, A. Iqbal, S. Huang, Z. Chen and X. Qian, *Mater. Chem. Phys.*, 2020, **250**, 123143.
36. J. D. Milshtein, A. P. Kaur, M. D. Casselman, J. A. Kowalski, S. Modekrutti, P. L. Zhang, N. Harsha Attanayake, C. F. Elliott, S. R. Parkin, C. Risko, F. R. Brushett and S. A. Odom, *Energy Environ. Sci*, 2016, **9**, 3531-3543.
37. J. Zhang, Z. Yang, I. A. Shkrob, R. S. Assary, S. o. Tung, B. Silcox, W. Duan, J. Zhang, C. C. Su and B. Hu, *Adv. Energy Mater*, 2017, **7**, 1701272.
38. G. Kwon, S. Lee, J. Hwang, H.-S. Shim, B. Lee, M. H. Lee, Y. Ko, S.-K. Jung, K. Ku, J. Hong and K. Kang, *Joule*, 2018, **2**, 1771-1782.
39. X. Wei, W. Xu, M. Vijayakumar, L. Cosimbescu, T. Liu, V. Sprenkle and W. Wang, *Adv. Mater.*, 2014, **26**, 7649-7653.
40. Y. Yan, S. G. Robinson, M. S. Sigman and M. S. Sanford, *J. Am. Chem. Soc.*, 2019, **141**, 15301-15306.
41. K. H. Hendriks, C. S. Sevov, M. E. Cook and M. S. Sanford, *ACS Energy Lett.*, 2017, **2**, 2430-2435.
42. J. Chai, A. Lashgari, X. Wang, C. K. Williams and J. J. Jiang, *J. Mater. Chem. A*, 2020, **8**, 15715-15724.
43. G. D. De La Garza, A. P. Kaur, I. A. Shkrob, L. A. Robertson, S. A. Odom and A. J. McNeil, *J. Mater. Chem. A*, 2022, 10, 18745-18752.
44. N. H. Attanayake, T. M. Suduwella, Y. Yan, A. P. Kaur, Z. Liang, M. S. Sanford and S. A. Odom, *J. Phys. Chem. C*, 2021, **125**, 14170-14179.
45. K. H. Hendriks, S. G. Robinson, M. N. Braten, C. S. Sevov, B. A. Helms, M. S. Sigman, S. D. Minteer and M. S. Sanford, *ACS cent. sci.*, 2018, **4**, 189-196.
46. E. C. Montoto, G. Nagarjuna, J. S. Moore and J. Rodríguez-López, *J. Electrochem. Soc.*, 2017, **164**, A1688.
47. Z. Liang, T. P. Nguyen, N. H. Attanayake, A. D. Easley, J. L. Lutkenhaus, K. L. Wooley and S. A. Odom, *Mater. Adv.*, 2022, **3**, 6558-6565.
48. Y. Ding, Y. Zhao, Y. Li, J. B. Goodenough and G. Yu, *Energy Environ. Sci*, 2017, **10**, 491-497.
49. J. Suttil, J. Kucharyson, I. Escalante-Garcia, P. Cabrera, B. James, R. Savinell, M. Sanford and L. Thompson, *J. Mater. Chem. A*, 2015, **3**, 7929-7938.
50. X. Wei, L. Cosimbescu, W. Xu, J. Z. Hu, M. Vijayakumar, J. Feng, M. Y. Hu, X. Deng, J. Xiao, J. Liu, V. Sprenkle and W. Wang, *Adv. Energy Mater*, 2015, **5**, 1400678.

51. N. H. Attanayake, Z. Liang, Y. Wang, A. P. Kaur, S. R. Parkin, J. K. Mobley, R. H. Ewoldt, J. Landon and S. A. Odom, *Mater. Adv.*, 2021, **2**, 1390-1401.
52. Z. Liang, N. H. Attanayake, K. V. Greco, B. J. Neyhouse, J. L. Barton, A. P. Kaur, W. L. Eubanks, F. R. Brushett, J. Landon and S. A. Odom, *ACS Appl. Energy Mater.*, 2021, **4**, 5443-5451.
53. A. Hollas, X. Wei, V. Murugesan, Z. Nie, B. Li, D. Reed, J. Liu, V. Sprenkle and W. Wang, *Nat. Energy*, 2018, **3**, 508-514.
54. B. Huskinson, M. P. Marshak, C. Suh, S. Er, M. R. Gerhardt, C. J. Galvin, X. Chen, A. Aspuru-Guzik, R. G. Gordon and M. J. Aziz, *Nature*, 2014, **505**, 195-198.
55. M. Wu, Y. Jing, A. A. Wong, E. M. Fell, S. Jin, Z. Tang, R. G. Gordon and M. J. Aziz, *Chem*, 2020, **6**, 1432-1442.
56. J. Luo, B. Hu, C. Debruler and T. L. Liu, *Angew. Chem. Int. Ed.*, 2018, **57**, 231-235.
57. C. DeBruler, B. Hu, J. Moss, J. Luo and T. L. Liu, *ACS Energy Lett.*, 2018, **3**, 663-668.
58. N. H. Attanayake, J. A. Kowalski, K. V. Greco, M. D. Casselman, J. D. Milshtein, S. J. Chapman, S. R. Parkin, F. R. Brushett and S. A. Odom, *Chem. Mater.*, 2019, **31**, 4353-4363.
59. L. Zhang, Y. Qian, R. Feng, Y. Ding, X. Zu, C. Zhang, X. Guo, W. Wang and G. Yu, *Nat. Commun*, 2020, **11**, 3843.
60. G. Kwon, K. Lee, M. H. Lee, B. Lee, S. Lee, S.-K. Jung, K. Ku, J. Kim, S. Y. Park, J. E. Kwon and K. Kang, *Chem*, 2019, **5**, 2642-2656.
61. J. Chai, A. Lashgari, Z. Cao, C. K. Williams, X. Wang, J. Dong and J. J. Jiang, *ACS Appl. Mater. Interfaces*, 2020, **12**, 15262-15270.
62. N. Amir, Y. Vestfrid, O. Chusid, Y. Gofer and D. Aurbach, *J. Power Sources*, 2007, **174**, 1234-1240.
63. A. J. MacLeod, *Appl. Math. Comput.*, 1993, **57**, 305-310.
64. J. D. Milshtein, J. L. Barton, R. M. Darling and F. R. Brushett, *J. Power Sources*, 2016, **327**, 151-159.
65. T. Janoschka, N. Martin, U. Martin, C. Friebe, S. Morgenstern, H. Hiller, M. D. Hager and U. S. Schubert, *Nature*, 2015, **527**, 78-81.
66. A. P. Kaur, K. C. Harris, N. H. Attanayake, Z. Liang, S. R. Parkin, M. H. Tang and S. A. Odom, *Chem. Mater.*, 2020, **32**, 3007-3017.
67. M. D. Casselman, A. P. Kaur, K. A. Narayana, C. F. Elliott, C. Risko and S. A. Odom, *Phys. Chem. Chem. Phys.*, 2015, **17**, 6905-6912.